

Autoregressive Neural TensorNet: Bridging Neural Networks and Tensor Networks for Quantum Many-Body Simulation

Zhuo Chen^{1,2} Laker Newhouse^{*3} Eddie Chen^{*4} Di Luo^{2,1,5} Marin Soljačić⁴

Abstract

Quantum many-body physics simulation has important impacts on understanding fundamental science and has applications to quantum materials design and quantum technology. However, due to the exponentially growing size of the Hilbert space with respect to the particle number, a direct simulation is intractable. While representing quantum states with tensor networks and neural networks are the two state-of-the-art methods for approximate simulations, each has its own limitations in terms of expressivity and optimization. To address these challenges, we develop a novel architecture, Autoregressive Neural TensorNet (ANTN), which bridges tensor networks and autoregressive neural networks. We show that Autoregressive Neural TensorNet parameterizes normalized wavefunctions with exact sampling, generalizes the expressivity of tensor networks and autoregressive neural networks, and inherits a variety of symmetries from autoregressive neural networks. We demonstrate our approach on the 2D J_1 - J_2 Heisenberg model with different systems sizes and coupling parameters, outperforming both tensor networks and autoregressive neural networks. Our work opens up new opportunities for both scientific simulations and machine learning applications.

1. Introduction

Quantum many-body physics is fundamental to our understanding of the universe. It appears in high energy physics where all the fundamental interactions in the Stan-

dard Model, such as quantum electrodynamics (QED) and quantum chromodynamics (QCD), are described by quantum mechanics. In condensed matter physics, quantum many-body physics has led to a number of rich phenomena and exotic quantum matters, including superfluids, superconductivity, the quantum Hall effect, and topological ordered states (Girvin & Yang, 2019). As an application, quantum many-body physics is crucial for new materials design. The electronic structure problem and chemical reactions in quantum chemistry are governed by quantum many-body physics. The recent development of quantum computers is also deeply connected to quantum many-body physics. A multi-qubit quantum device is intrinsically a quantum many-body system, such that progress on quantum computer engineering is tied to our understanding of quantum many-body physics (Preskill, 2021).

All information of a closed quantum many-body system is captured by the wavefunction, whose properties are described by the famous Schrödinger equation. An important tool to study and understand quantum many-body physics is to classically simulate the wavefunction. However, the wavefunction is a mathematical object in Hilbert space, the dimension of which grows exponentially with the number of particles. For example, for the spin-1/2 particle with two degree of freedom, the wavefunction of 300 spins will have dimension 2^{300} , which is larger than the number of particles in the observable universe. Furthermore, the Schrödinger equation is a complex-valued high-dimensional equation, which is challenging to solve or simulate in general.

A number of algorithms have been developed to simulate quantum many-body physics, including quantum Monte Carlo, tensor networks, neural network quantum states, and direct quantum computation. In particular, computing the ground state of quantum many-body systems is of great interest. One important approach is the variational principle, which provides an upper bound for the ground state energy. To apply variational principle successfully, one must design an ansatz that can represent and optimize the wavefunction efficiently. Tensor networks and neural network quantum states (Carleo & Troyer, 2017) are the two main state-of-the-art methods that can be applied with the variational principle for quantum many-body simulation. However,

^{*}Equal contribution ¹Center for Theoretical Physics, Massachusetts Institute of Technology ²NSF AI Institute for Artificial Intelligence and Fundamental Interactions ³Department of Mathematics, Massachusetts Institute of Technology ⁴Department of Physics, Massachusetts Institute of Technology ⁵Department of Physics, Harvard University. Correspondence to: Di Luo <diluo@mit.edu>.

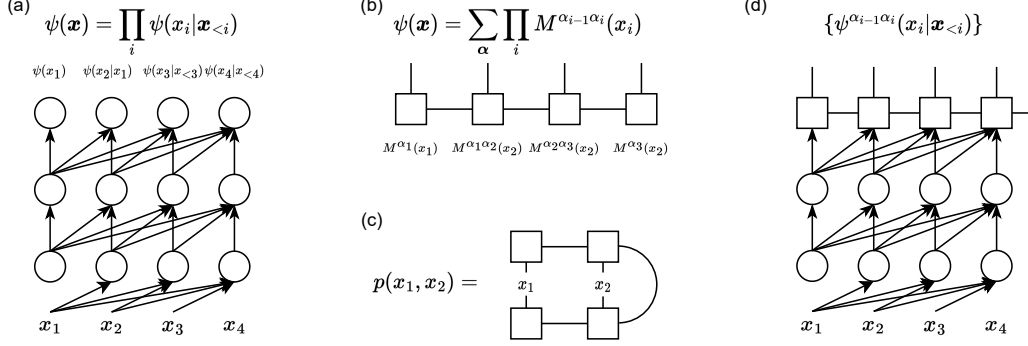


Figure 1. Diagram of (a) an autoregressive neural network, (b) a matrix product state tensor network, (c) a marginal probability of a matrix product state tensor network and (d) an autoregressive neural tensor network. We illustrate a fully connected autoregressive neural network here, but any autoregressive neural network can be used to build the autoregressive neural tensor network.

tensor networks usually suffer from an expressivity issue in higher dimensional systems, while neural network quantum states usually lack the inductive bias from the underlying physics structure and have sign structure challenges in the representation.

In this paper, we develop a novel architecture, Autoregressive Neural TensorNet (ANTN), to bridge neural network quantum states and tensor networks, achieving the best of both worlds. In particular, our contributions are threefold:

- Develop Autoregressive Neural TensorNet with two variants called “elementwise” and “blockwise,” which each naturally generalize the two state-of-the-arts ansatzes, tensor networks and autoregressive neural networks.
- Prove that Autoregressive Neural TensorNet is normalized with exact sampling, is more expressive than tensor networks and autoregressive neural networks, and inherits multiple symmetries from autoregressive neural networks.
- Demonstrate our methods on the 2D J_1 - J_2 Heisenberg model, outperforming both tensor networks and autoregressive neural networks.

2. Related Work

Tensor Network. A high dimensional wavefunction in a spin system is equivalent to a high rank tensor. The key insight of tensor networks is to approximate the high dimensional wavefunction with a low rank tensor decomposition. Famous examples of tensor networks include matrix product state (MPS) (Vidal, 2003; 2004), PEPS (Verstraete & Cirac, 2004), and MERA (Vidal, 2007). Tensor networks are physically motivated and capture the entanglement structure of the underlying physical system. One well-known algorithm associated with MPS is the density matrix renormalization group (DMRG) (White, 1992). It can efficiently solve the

ground state of 1D gapped states due to the area law, which states that such systems have constant entanglement. Tensor networks are a state-of-the-art method and have been applied to simulate ground states, finite-temperature physics, and real-time dynamics in various systems. Despite the advancement of tensor networks over the years, their multilinear property could pose challenges to applying the method to higher dimensional systems and real-time dynamics when the entanglement requirement is high; these are the scenarios in which tensor networks are not expressive enough.

In the computer science and machine learning community, tensor networks also appear under different tensor decomposition methods, including tensor train (Oseledets, 2011) and CP decomposition. Tensor train is equivalent to MPS mathematically. Tensor network methods have also been applied to various machine learning tasks.

Neural Network Quantum State (NNQS). The key idea of the neural network quantum state (NNQS) is to represent the high dimensional wavefunction with an expressive neural network. Pioneering work (Carleo & Troyer, 2017) was first proposed by Giuseppe and Tryan to solve the ground states of the quantum spin systems with the restricted Boltzman machine (RBM). It has been shown that a large family of quantum states (Sharir et al., 2021) can be well approximated by NNQS and exactly represented (Gao & Duan, 2017; Lu et al., 2019; Levine et al., 2019a; Luo et al., 2021b;a; Deng et al., 2017; Huang & Moore, 2021; Vieijra et al., 2020). Furthermore, any quantum state supervised learning with NNQS is guaranteed to converge in the infinite width limit (Luo & Halverson, 2021). Recently, NNQS has been shown to achieve state-of-the-art results for computing ground states and the real time dynamics properties of closed and open quantum systems (Gutiérrez & Mendl, 2020; Schmitt & Heyl, 2020; Vicentini et al., 2019; Yoshioka & Hamazaki, 2019; Hartmann & Carleo,

2019; Nagy & Savona, 2019; Luo et al., 2021b; 2022a), with applications to a variety of fields including condensed matter physics (Han & Hartnoll, 2020; Pfau et al., 2020; Choo et al., 2019; Hibat-Allah et al., 2020; Luo & Clark, 2019; Hermann et al., 2019; Wang et al., 2021; Glasser et al., 2018; Stokes et al., 2020; Nomura et al., 2017; Astrakhantsev et al., 2021), high energy physics (Luo et al., 2021a;b; Adams et al., 2021; Martyn et al., 2022; Chen et al., 2022; Luo et al., 2021b; 2022b), and quantum information science (Medvidović & Carleo, 2021; Carrasquilla et al., 2019; Torlai et al., 2018).

An important advancement of NNQS came from the development of autoregressive neural network quantum states. Since neural networks methods such as RBM or convolutional neural networks (CNN) are not normalized, they usually require Markov Chain Monte Carlo (MCMC) for sampling during the optimization, which can result in long auto-correlation time and noisy estimation of gradients. In contrast, autoregressive neural network quantum states represent the wavefunction with a conditional wavefunction so that they are self-normalized with exact sampling, which is much more sample efficient and provides better gradient estimation. It has been shown that autoregressive neural network quantum states, such as PixelCNN, RNN and transformer wavefunctions, could have more expressivity than RBM and achieve state-of-the-art performance (Luo et al., 2021b; Hibat-Allah et al., 2020). Since symmetry plays a crucial role in quantum many-body physics, another advancement of NNQS is to develop neural networks that obey the underlying symmetries of the system, including translational symmetry (Choo et al., 2019), discrete rotational symmetry (Choo et al., 2019), global U(1) symmetry (Hibat-Allah et al., 2020), anti-symmetry (Luo & Clark, 2019; Hermann et al., 2019; Pfau et al., 2020), and gauge symmetries (Luo et al., 2021a; 2022b; 2021b; Chen et al., 2022).

Even though NNQS has been shown to have great potential to advance quantum many-body simulation, there are several challenges to be resolved, such as the sign structure problem and the lack of physical prior. Recently, one attempt to address these challenges has been to integrate neural networks with a physically motivated ansatz such as a tensor network. (Lami et al., 2022) has proposed matrix product state with neural network backflow, which integrates MPS with RBM and (Wu et al., 2022) generalizes MPS to RNN with a multilinear memory update. However, the former construction can not produce normalized wavefunctions, while the latter construction does not have the nonlinearity of standard neural network wavefunctions.

3. Architecture

In this work, we focus on spin- $\frac{1}{2}$ systems in quantum many-body physics. The wavefunction or quantum state ψ of the system is a function $\psi : \mathbb{Z}_2^n \rightarrow \mathbb{C}$, where n is the system size. The input \mathbf{x} to the wavefunction is an n -bit string taking a value of 0 or 1 on each bit. Because the size of wavefunction grows exponentially with the system size n , a direct computation quickly becomes intractable. The goal of the neural network quantum state is to design a compact architecture that can approximate and optimize the wavefunction efficiently.

3.1. Preliminaries

Autoregressive Neural Network Wavefunction. The standard autoregressive neural network generates the full probability distributions as a product of conditional distributions as

$$p(\mathbf{x}) = \prod_{i=1}^n p(x_i | \mathbf{x}_{<i}), \quad (1)$$

where $\mathbf{x} = (x_1, \dots, x_n)$ is a configuration of n particles, $\mathbf{x}_{<i} = (x_1, \dots, x_{i-1})$ is any configuration before x_i , and $p(x_i | \mathbf{x}_{<i})$ is the conditional probability that satisfies the normalization condition $\sum_{x_i} p(x_i | \mathbf{x}_{<i}) = 1$. To represent a (normalized) quantum wavefunction, it is standard to replace $p(x_i | \mathbf{x}_{<i})$ with $\psi(x_i | \mathbf{x}_{<i})$, which allows complex values and has a different normalization condition $\sum_{x_i} |\psi(x_i | \mathbf{x}_{<i})|^2 = 1$ (Sharir et al., 2020; Hibat-Allah et al., 2020; Luo et al., 2021b) (Fig. 1 (a)).

Theorem 3.1. *Autoregressive neural network quantum wavefunction is normalized and allows for exact sampling.*

Proof. See Appendix A.1.

Because of its normalization and exact sampling, the autoregressive neural network can be more efficient when training and computing various quantum observables compared to other generative neural networks.

Matrix Product State. Matrix product state (MPS) (also known as tensor train) is a widely used tensor network architecture to study quantum many body physics (Vidal, 2003; 2004). The MPS defines a wavefunction by contracting tensors as

$$\psi(\mathbf{x}) = \sum_{\alpha} \prod_{i=1}^n M^{\alpha_{i-1} \alpha_i}(x_i), \quad (2)$$

where $M^{\alpha_{i-1} \alpha_i}(x_i)$ is a rank three tensor, with α_i and α_{i+1} the left and right bond dimension of the tensor ($\mathcal{D}(\alpha_0) = \mathcal{D}(\alpha_{n+1}) = 1$ and are not summed over for open boundary condition) (Fig. 1 (b)). Because of the gauge symmetry, the same wavefunction can be represented with different choices of M tensors. Canonical forms (right canonical

form (Ferris & Vidal, 2012) here specifically) can be chosen to fix the tensors, which allows the marginal probability to be computed efficiently (Fig. 1 (c)).

Theorem 3.2. *Matrix product state wavefunction is normalized and allows for exact sampling in right canonical form.*

Proof. See Appendix A.2.

3.2. Autoregressive Neural TensorNet (ANTN)

Both autoregressive neural networks and MPS are powerful ansatzes for parameterizing quantum many-body wavefunctions. However, they could cover different spaces in the Hilbert space. Because both these ansatzes allow for exact sampling, it is natural to combine them to produce a more powerful ansatz. Therefore, we develop the Autoregressive Neural TensorNet (ANTN) (Fig. 1 (d)). In the last layer of the ANTN, instead of outputting the conditional wavefunction $\psi(x_i|\mathbf{x}_{<i})$, we output an (unnormalized) conditional wavefunction tensor $\tilde{\psi}^{\alpha_{i-1}\alpha_i}(x_i|\mathbf{x}_{<i})$ for each site. Let's define the left partially contracted tensor analogous to MPS in Appendix A.2 as $\tilde{\psi}_L^{\alpha_j}(\mathbf{x}_{\leq j}) := \sum_{\alpha_{\leq j}} \prod_{i=1}^j \tilde{\psi}^{\alpha_{i-1}\alpha_i}(x_i|\mathbf{x}_{<i})$. The (unnormalized) marginal probability distribution is also defined analogous to MPS as

$$q(\mathbf{x}_{\leq j}) := \sum_{\alpha_j} \tilde{\psi}_L^{\alpha_j}(\mathbf{x}_{\leq j}) \tilde{\psi}_L^{\alpha_j}(\mathbf{x}_{\leq j})^*, \quad (3)$$

where $*$ denotes complex conjugation. The conditional probability can be obtained by normalization as $q(x_j|\mathbf{x}_{<j}) = q(\mathbf{x}_{\leq j}) / \sum_{x_j} q(\mathbf{x}_{\leq j})$. The overall wavefunction is then defined as

$$\psi(\mathbf{x}) := \sqrt{q(\mathbf{x})} e^{i\phi(\mathbf{x})}, \quad (4)$$

with $q(\mathbf{x}) := \prod_{i=1}^n q(x_i|\mathbf{x}_{<i})$ and the phase $\phi(\mathbf{x}) := \text{Arg} \sum_{\alpha} \prod_{i=1}^n \tilde{\psi}^{\alpha_{i-1},\alpha_i}(x_i|\mathbf{x}_{<i})$. In other words, we define the amplitude of the wavefunction through the conditional probability distributions and define the phase analogous to the standard MPS.

Elementwise and Blockwise Construction for ANTN. We develop two different constructions for ANTN that differ in the last layer where the neural network outputs the tensors.

The elementwise ANTN is given by

$$\tilde{\psi}^{\alpha_{i-1}\alpha_i}(x_i|\mathbf{x}_{<i}) = M^{\alpha_{i-1}\alpha_i}(x_i) + f_{NN}^{\alpha_{i-1}\alpha_i}(x_i|\mathbf{x}_{<i}), \quad (5)$$

where $f_{NN}^{\alpha_{i-1}\alpha_i}(x_i|\mathbf{x}_{<i})$ is the output with complex number from an autoregressive neural network. The blockwise ANTN is given by

$$\tilde{\psi}^{\alpha_{i-1}\alpha_i}(x_i|\mathbf{x}_{<i}) = M^{\alpha_{i-1}\alpha_i}(x_i) + f_{NN}(x_i|\mathbf{x}_{<i}), \quad (6)$$

where $f_{NN}(x_i|\mathbf{x}_{<i})$ is the output with complex number from an autoregressive neural network. This results in a lower complexity which allows us to use a larger maximum bond dimension for MPS.

PixcelCNN TensorNet. Our construction above is general and can be applied to any autoregressive neural network. Depending on the application, we can use different autoregressive neural network architectures. Because PixelCNN is good at capturing 2D correlations, we integrate it with MPS to develop the PixelCNN TensorNet. The PixelCNN we use is the gated PixelCNN (Van den Oord et al., 2016b) implemented in (Chen et al., 2022). We will apply PixcelCNN TensorNet for the simulations of the 2D J_1 - J_2 Heisenberg model later. We note that the elementwise and the blockwise construction can both be applied to PixcelCNN TensorNet.

4. Theoretical Results

4.1. Sampling and Complexity Results of ANTN

Theorem 4.1. *The ANTN wavefunction is normalized and allows for exact sampling.*

Proof. This is a direct consequence that we defined the amplitude of the wavefunction through conditional probability distributions. By normalizing the individual conditional probability distributions and sampling from them, both conditions are satisfied. \square

We need to notice that because we are not enforcing the canonical form as we define the wavefunction, in general, $\psi(\mathbf{x}) \neq \sum_{\alpha} \prod_{i=1}^n \tilde{\psi}^{\alpha_{i-1}\alpha_i}(x_i|\mathbf{x}_{<i})$ unless the canonical form is satisfied by chance. Nevertheless, this does not affect the validity of the wavefunction nor the expressiveness of the neural network. More details about exact sampling can be found in Appendix C

Complexity Analysis. We first note that for matrix product states, the number of parameters and computational complexity for evaluating a bitstring \mathbf{x} scales as $O(n\chi^2)$, where n is the number of particles and χ is the bond dimension of MPS with α the index ($1 \leq \alpha \leq \chi$). The sampling complexity scales as $O(n^2\chi^2)$. The DMRG algorithm has a computational complexity of $O(n\chi^3)$ (White, 1992).

For PixelCNN, the complexity of evaluating a bitstring \mathbf{x} is $O(ndh_{\text{dim}}^2)$, while the complexity of sampling a bitstring is $O(n^2dh_{\text{dim}}^2)$, where d is the depth of the CNN and h_{dim} is the hidden dimension. The Autoregressive Neural TensorNet inherits the memory complexity and the computational complexity of the underlying autoregressive neural network. In addition, since the last layer of the autoregressive neural network needs to output the tensor correction, we must account for some additional parameters. Assuming the last layer of the autoregressive neural network has the same hidden dimension h_{dim} , we find that for the elementwise

ANTN with bond dimension χ , the final layer adds an additional $O(n\chi^2 h_{\text{dim}})$ parameters, resulting in total parameters scaling as

$$O(n_{\text{ARNN}} + n\chi^2 h_{\text{dim}}), \quad (7)$$

where n_{ARNN} is the number of parameters of the underlying autoregressive neural network.

The final layer also adds the same $O(n\chi^2 h_{\text{dim}})$ computational steps for evaluation and $O(n^2\chi^2 h_{\text{dim}})$ steps for sampling, which results in a computational complexity scaling as

$$O(n^\gamma(dh_{\text{dim}}^2 + \chi^2 h_{\text{dim}})), \quad (8)$$

with $\gamma = 1$ for evaluation and $\gamma = 2$ for sampling.

For the blockwise ANTN, the final layer adds $O(nh_{\text{dim}})$ parameters and no additional computational steps, resulting in total number of parameters that scales as

$$O(n_{\text{ARNN}} + n\chi^2 + nh_{\text{dim}}), \quad (9)$$

and total computational complexity that scales as

$$O(n^\gamma(dh_{\text{dim}}^2 + \chi^2)), \quad (10)$$

with $\gamma = 1$ for evaluation and $\gamma = 2$ for sampling.

We note that while in our current implementation, $\gamma = 2$ for sampling, it is possible to reduce it to $\gamma = 1$ by cleverly storing the partial results.

The difference in computational complexities and number of parameters between elementwise ANTN and blockwise ANTN implies that blockwise ANTN is usually more economical than elementwise ANTN for the same h_{dim} and χ . Therefore, for small bond dimension, we use the elementwise ANTN for a more flexible parameterization with a higher cost. In contrast, for large bond dimension we use the blockwise ANTN, which saves computational complexity and improves the initial performance (with DMRG initialization) of the blockwise ANTN at the cost of less flexible modifications from the autoregressive neural network. We also note that compared to the state-of-the-arts MPS simulation, even for our blockwise ANTN, it may have much smaller bond dimension. For example, in the later experimental section, we use bond dimension 70 for blockwise ANTN while the best DMRG results use bond dimension 1024, which has much more parameters than our ANTN. In general, our ANTN has much fewer parameters compared to matrix product state due to the $O(\chi^2)$ parameters scaling which dominates at large bond dimension.

4.2. Expressivity Results of ANTN

Theorem 4.2. *Autoregressive Neural TensorNet has generalized expressivity over tensors network and autoregressive neural networks.*

Proof. If we set $\mathcal{D}(\alpha_i) = 1$ for all i , the marginal probability distribution in Eq. 3 reduces to that of the standard autoregressive neural network (up to normalization). This means both the conditional and overall probability distributions are the same. The phase of the ATNT becomes a sum of the phases of each conditional wavefunction, which also reduces to the autoregressive neural network. This implies that autoregressive neural networks are a special case of ANTN.

If we set $f_{NN}^{\alpha_{i-1}\alpha_i}(x_i|\mathbf{x}_{<i}) = 0$ in Eq. 5 and $f_{NN}(x_i|\mathbf{x}_{<i}) = 0$ in Eq. 6, then Autoregressive Neural TensorNet reduces to the tensor network shown in Eq. 2. This implies that tensor networks are a special case of ANTN. Thus ANTN generalizes both autoregressive neural networks and tensor networks with more expressivity. \square

Theorem 4.3. *Autoregressive Neural TensorNet can have volume law entanglement, which is strictly beyond the expressivity of matrix product state.*

Proof. We have proven that ANTN can be reduced to an autoregressive neural network, which has been shown to have volume law entanglement that can not be efficiently represented by tensor networks (Sharir et al., 2021; Levine et al., 2019b). Hence, ANTN cannot in general be represented by matrix product state efficiently and it has strictly greater expressivity. \square

4.3. Symmetry Results of ANTN

Symmetry plays an important role in quantum many-body physics and quantum chemistry. Many of the symmetries can be enforced in autoregressive neural networks via the two classes of the symmetries—*mask symmetry* and *function symmetry*. Here, we show that ANTN inherits the symmetries from autoregressive neural networks.

Definition 4.1 (Mask Symmetry). A conditional wavefunction $\psi(x_i|\mathbf{x}_{<i})$ has a *mask symmetry* if $\psi(x_i|\mathbf{x}_{<i}) = 0$ for some x_i given $\mathbf{x}_{<i}$.

Definition 4.2 (Function Symmetry). For a function F that satisfies $\{F(x_i), F(\mathbf{x}_{<i})\} = F(\mathbf{x}_{\leq i})$, a conditional wavefunction tensor $\psi(x_i|\mathbf{x}_{<i})$ has a *function symmetry* over the F if $\psi(x_i|\mathbf{x}_{<i}) = \psi(F(x_i)|F(\mathbf{x}_{<i}))$.

Here, $F(x_i)$ is allowed to depend on $\mathbf{x}_{<i}$.

Theorem 4.4. *Autoregressive Neural TensorNet inherits mask symmetry and function symmetry from autoregressive neural networks.*

Proof. We want to show that if an ANTN is built from an autoregressive neural network with mask symmetry and function symmetry, the ANTN inherits the mask symmetry and the function symmetry.

For mask symmetry, we can apply the same mask, which sets $\psi(x_i|\mathbf{x}_{<i}) = 0$ in the standard autoregressive neural

network, directly on the conditional probability $q(x_j|x_{<i})$ of the ANTN. This guarantees the mask symmetry.

For function symmetry, one can apply the function symmetry to the left partially contracted tensor instead of the scalar in the case of the autoregressive neural network. This results in the same function symmetry on both the conditional probabilities and the phase. See Appendix A.3 for a detailed proof. \square

Notice that while the mask symmetry can also be applied to the tensors as the function symmetry, the function symmetry cannot be directly applied to the conditional probabilities. This is because the conditional probabilities (and marginal probabilities) at site i for the ANTN are constructed by contracting all the tensors at sites $\leq i$. Thus, without applying on tensor level, the function symmetry on site i cannot have desired effect on sites after i .

Corollary 4.4.1 (Global U(1) Symmetry). *Autoregressive Neural TensorNet can realize global U(1) symmetry, which conserves particle number.*

Proof. A global U(1) symmetry in a spin system manifest as a conservation of the sum of spin up and spin down, equivalently, $\psi(\mathbf{x}) = 0$ for \mathbf{x} violates such conservation. (Hibat-Allah et al., 2020) has shown that autoregressive neural networks can preserve global U(1) symmetry as a mask symmetry, which ANTN inherits. \square

Corollary 4.4.2 (\mathbb{Z}_2 Spin Flip Symmetry). *Autoregressive Neural TensorNet can realize \mathbb{Z}_2 spin flip symmetry such that the ANTN wavefunction is invariant under conjugation of the input.*

Proof. Spin flip symmetry exists for quantum chemistry systems that do not couple spin up and spin down electron, so that the wave function is invariant to inputs which spin up and down are flipped. (Barrett et al., 2022) has shown that autoregressive neural network can preserve \mathbb{Z}_2 spin flip symmetry as a function symmetry, which ANTN inherits. \square

Corollary 4.4.3 (Discrete Abelian and Non-Abelian Symmetries). *Autoregressive Neural TensorNet can realize discrete Abelian and Non-Abelian symmetries.*

Proof. Gauge symmetry is a local symmetry such that the function is invariant under local transformation. (Luo et al., 2021b) has shown that autoregressive neural network can preserve discrete abelian and non-Abelian symmetries as either the mask symmetry or the function symmetry, which ANTN inherits. \square

5. Algorithms

5.1. Quantum Preliminaries

For spin systems or fermionic systems in the second quantization, the input \mathbf{x} to wavefunction is an n -bit string, where n is the system size. Therefore, the wavefunction ψ can be viewed as a complex-valued vector of size 2^n . With Dirac notation $\langle \psi |$ and $|\psi \rangle$ correspond to a conjugate row vector and a column vector respectively. The expression $\psi(\mathbf{x})$ is an element of the vector with \mathbf{x} acting as an index. A Hamiltonian \hat{H} is a Hermitian matrix of size $2^n \times 2^n$ that acts on the wavefunction by matrix-vector multiplication. The notation $\langle \psi | \hat{H} | \psi \rangle$ indicates the inner product between the conjugate of ψ and $\hat{H}\psi$.

5.2. Variational Monte Carlo

For a given Hamiltonian \hat{H} , the variational principle in quantum mechanics provides an upper bound on the ground state energy E_g . For all (normalized) wavefunctions $|\psi\rangle$, it gives

$$E_g \leq \langle \psi | \hat{H} | \psi \rangle. \quad (11)$$

For a given normalized wavefunction $|\psi_\theta\rangle$, we can stochastically evaluate the expectation of energy for a Hamiltonian \hat{H} as

$$\langle \psi_\theta | \hat{H} | \psi_\theta \rangle \approx \frac{1}{N_s} \sum_{\mathbf{x} \sim |\psi_\theta|^2}^{N_s} \frac{\hat{H}\psi_\theta(\mathbf{x})}{\psi_\theta(\mathbf{x})} \equiv \frac{1}{N_s} \sum_{\mathbf{x} \sim |\psi_\theta|^2}^{N_s} E_{\text{loc}}(\mathbf{x}), \quad (12)$$

where N_s is the batch size. The gradient with respect to the energy is given by (see (Luo et al., 2021b) for derivation)

$$\frac{\partial}{\partial \theta} \langle \psi_\theta | \hat{H} | \psi_\theta \rangle \approx \frac{2}{N_s} \sum_{\mathbf{x} \sim |\psi_\theta|^2}^{N_s} \Re \left\{ E_{\text{loc}}(\mathbf{x}) \frac{\partial}{\partial \theta} \log \psi_\theta^*(\mathbf{x}) \right\}. \quad (13)$$

The variance control (Greensmith et al., 2004) can be further applied to replace $E_{\text{loc}}(\mathbf{x})$ in the gradient formula with

$$E'_{\text{loc}}(\mathbf{x}) = E_{\text{loc}}(\mathbf{x}) - \frac{1}{N} \sum_{\mathbf{x} \sim |\psi_\theta|^2}^N E_{\text{loc}}(\mathbf{x}). \quad (14)$$

To see how the variance control works, one can consider the case that ψ_θ is the exact ground state ψ_g . In this case ψ_θ should produce no gradient for any samples. Even though Eq. 13 is zero when \mathbf{x} is summed over the whole Hilbert space, it is not zero for any given single sample. By contrast, Eq. 14 demonstrates a zero gradient for any single sample.

Conventional variational Monte Carlo uses the Markov-chain Monte Carlo method, which can suffer from a long auto-correlation time. In contrast, our Autoregressive Neural TensorNet can perform exact sampling to generate independent samples and provide a more accurate gradient estimate.

$J_2 = 0.2$	DMRG (1024)	DMRG (70)	DMRG (8)	PixelCNN	Elementwise (8)	Blockwise (70)
8×8	-2.236804	-2.192334	-2.001620	-2.21218(16)	-2.23690(4)	-2.23484(73)
10×10	-2.255633	-2.191048	-1.997537	-2.22462(24)	-2.26034(6)	-2.257550(78)
12×12	-2.264084	-2.185071	-1.998207	-2.24311(102)	-2.27446(27)	-2.26152(50)
$J_2 = 0.5$	DMRG (1024)	DMRG (70)	DMRG (8)	PixelCNN	Elementwise (8)	Blockwise (70)
8×8	-1.934127	-1.885860	-1.735175	-1.77058(29)	<u>-1.93018(8)</u>	-1.93000(7)
10×10	-1.938770	-1.866159	-1.734326	-1.74098(29)	-1.94001(6)	-1.93842(42)
12×12	-1.931243	-1.851954	-1.735906	-1.74282(30)	-1.94686(6)	-1.94298(43)
$J_2 = 0.8$	DMRG (1024)	DMRG (70)	DMRG (8)	PixelCNN	Elementwise (8)	Blockwise (70)
8×8	-2.016361	-1.967760	-1.833780	-1.93825(16)	<u>-2.00036(16)</u>	-1.99148(13)
10×10	-2.062730	-2.007845	-1.869871	-1.98331(17)	<u>-2.05707(43)</u>	-2.05088(14)
12×12	-2.093013	-2.030131	-1.893916	-2.03226(59)	-2.09457(10)	-2.09113(43)

Table 1. Performance of PixelCNN, elementwise ANTN, and blockwise ANTN on ground state energy per site calculations of 2D Heisenberg Hamiltonians with J_2 coefficients of 0.2, 0.5, and 0.8. The best energy is bolded in each row. The best TensorNet energy is underlined in each row. The DMRG and TensorNet models depend on the bond dimension in parentheses. DMRG results in small system sizes with a bond dimension of 1024 are close to exact.

With the gradient obtained from Eq. 13, one can perform gradient descent on the parameter to obtain

$$\theta_{t+1} = \theta_t - \eta \frac{\partial}{\partial \theta_t} \langle \psi_{\theta_t} | \hat{H} | \psi_{\theta_t} \rangle, \quad (15)$$

where θ_t is the parameter in step t and η is the learning rate.

Complexity Analysis. The complexity of computing gradients through Eq. 13 comes from both the sampling complexity of ANTN and the evaluation complexity of the local energy $E_{loc}(\mathbf{x}) = \frac{\hat{H}\psi(\mathbf{x})}{\psi(\mathbf{x})}$. Since \hat{H} usually involves multiple Pauli operators with number M , the evaluation complexity dominates over the exact sampling complexity of ANTN. The gradient complexity scales with $O(N_s N_c n_{eva})$, where n_{eva} is the evaluation complexity of ANTN per configuration and N_c is the number of non zero configurations \mathbf{x} in $\langle \mathbf{x} | \hat{H} | \mathbf{x} \rangle$ for a given y . With n as the system size, in the 2D J_1 - J_2 Heisenberg model, we have $N_c \sim O(n)$.

DMRG Initialization. Since our Autoregressive Neural TensorNet generalizes from tensor network, both the elementwise and the blockwise can take advantage of the DMRG optimization (White, 1992) as an initialization. In practice, we can initialize the tensor network component with the optimized DMRG results with the same bond dimension (similar to (Lami et al., 2022; Wu et al., 2022)). This is a nice feature since it provides a good sign structure and inductive bias from physics structure, which does not exist in the conventional autoregressive neural network.

6. Experiments

Experimental Setup. We consider the 2D J_1 - J_2 Heisenberg model with open boundary condition. The model has a rich phase diagram with at least three different phases

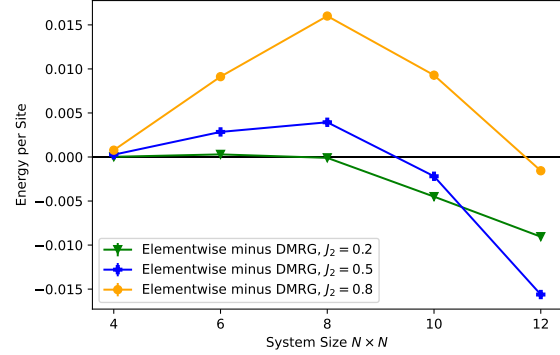


Figure 2. Energy per site difference between elementwise Autoregressive Neural TensorNet and DMRG with bond dimension 1024 (lower is better). The concavity of each plot demonstrates that elementwise ANTN scales better than DMRG for large systems.

across different J_2/J_1 values (Capriotti et al., 2004) (Lante & Parola, 2006). In addition, the complicated structure of its ground state makes it a robust model on which to test state-of-the-art methods.

The 2D J_1 - J_2 Hamiltonian is given by

$$H = J_1 \sum_{\langle i,j \rangle} \vec{S}_i \cdot \vec{S}_j + J_2 \sum_{\langle\langle i,j \rangle\rangle} \vec{S}_i \cdot \vec{S}_j, \quad (16)$$

where $\langle i,j \rangle$ is the nearest neighbour, $\langle\langle i,j \rangle\rangle$ is the next nearest neighbour, and $\vec{S}_i \cdot \vec{S}_j = X_i \otimes X_j + Y_i \otimes Y_j + Z_i \otimes Z_j$. Here X , Y and Z are the Pauli matrices defined by

$$X = \begin{bmatrix} 0 & 1 \\ 1 & 0 \end{bmatrix}, \quad Y = \begin{bmatrix} 0 & -i \\ i & 0 \end{bmatrix}, \quad Z = \begin{bmatrix} 1 & 0 \\ 0 & -1 \end{bmatrix}. \quad (17)$$

In this experiment, we compare the performance of six mod-

els to compute the ground state energy of the J_1 - J_2 Hamiltonian system with $J_1 = 1$ and ratios $J_2/J_1 = 0.2, 0.5, 0.8$, corresponding to three different phases. The first three models are tensor networks, using a density matrix renormalization group (DMRG) with bond dimensions of 8, 70, and 1024. For small system sizes, the DMRG results with bond dimension 1024 may be regarded as a benchmark. The fourth model is a PixelCNN pure neural network; the fifth and sixth models are elementwise and blockwise Autoregressive Neural TensorNet models. Thus the experiment compares our novel architecture (fifth and sixth models) against the two previous state-of-the-art techniques (first through fourth models).

Metric. Since our approach is based on the variational principle discussed in Sec. 5, it provides an upper bound on the exact ground state energy; therefore, the lower the energy, the better. Since the DMRG with bond dimension 1024 should represent a system of 20 spins exactly, it becomes close to the exact results in small system size.

Results and Discussion. Table 1 summarizes the ground state energy computed by the different models at different J_2/J_1 ratios in three distinct phases. The results communicate three important messages.

First, the elementwise and blockwise Autoregressive Neural TensorNet models consistently outperform the pure neural network PixelCNN model. This agrees with Theorem 4.2 that both elementwise and blockwise ANTN have greater expressivity than autoregressive neural networks.

Second, in all cases the Autoregressive Neural TensorNets surpass the corresponding DMRG on which they are based. For example, even in the 8×8 system size with the $J_2 = 0.5$ Hamiltonian in which DMRG 1024 outperforms the elementwise ANTN, the elementwise ANTN still significantly improves on the base DMRG 8 result from which it began. It is consistent with Theorem. 4.2 and Theorem. 4.3 that ANTN is more expressive than tensor network.

Third, and most importantly, the Autoregressive Neural TensorNet models scale well for larger systems. Compared to DMRG, the elementwise and blockwise Autoregressive Neural TensorNet models continue to compute lower ground state energies even as the system size grows larger. This is important because the DMRG memory cost is dominated by the bond dimension χ , which limits its use in practice for large system sizes. According to the complexity analysis in Sec. 4.1, ANTN has lower complexity than tensor network and thus scales better for larger systems.

Figure 2 visualizes the scalability of Autoregressive Neural TensorNets compared to DMRG. The figure plots the difference in computed energy between the elementwise ANTN and DMRG with bond dimension 1024. Lower energies signify better performance for the elementwise ANTN. As

the system size increases, the elementwise ANTN outperforms DMRG in all cases. We notice that for large J_2 , the system goes into a stripped phase (Nomura & Imada, 2021), which can be less challenging for DMRG calculation. Nevertheless, our ANTN still outperforms DMRG on the 12×12 system.

We note that our results at $J_2 = 0.5$ on a system size of 8×8 outperform the recently developed method of matrix product state backflow, which integrates MPS with Restricted Boltzmann Machines (Lami et al., 2022). We also provide additional benchmarks with other ansatz as well as at $J_2 = 0$ in Appendix B.

Our results provide strong evidence that Autoregressive Neural TensorNets integrating tensor networks and autoregressive neural networks perform more powerfully than either individually, achieving state-of-the-art results.

7. Conclusion and Future Work

In this paper, we developed Autoregressive Neural TensorNet, bridging the two state-of-the-art methods in the field, tensor networks and autoregressive neural networks. We proved that Autoregressive Neural TensorNet is self-normalized with exact sampling, naturally generalizes the expressivity of both tensor networks and autoregressive neural networks, and inherits various symmetries from autoregressive neural networks. We demonstrated our approach on the challenging 2D J_1 - J_2 Heisenberg model with different system sizes and couplings. Our results achieve better performance than both the original tensor network and autoregressive neural network while surpassing tensor networks with large bond dimension as the system size increases. Meanwhile, we would also like to discuss a few limitations of the current work and the future directions.

First, in this paper, we only integrated the PixelCNN with MPS. While PixelCNN is a powerful autoregressive neural network in 2D, MPS can be limited in 2D. Nevertheless, our approach is general and would work with arbitrary autoregressive neural network and tensor network for any spatial dimension and boundary condition. One fruitful direction would be to investigate the combination from other powerful autoregressive neural networks such as RNNs and Transformers, together with more advanced tensor networks such as MERA and PEPS. More powerful component networks will allow the design of more flexible and expressive Autoregressive Neural TensorNets dependent on different dimensionality and correlation of the physical system.

Second, while we applied our approach for the challenging 2D J_1 - J_2 Heisenberg model and achieved better than state-of-the-art performance, it will be of great interest to explore the applicability of our methods to other systems in high energy physics, condensed matter physics and quantum

chemistry.

Third, although this work focuses on ground state problems, our approach can be naturally extended to finite-temperature and real-time simulations, taking advantage of existing algorithms for both tensor networks and autoregressive neural networks in those contexts. Since we have proved that Autoregressive Neural TensorNet has greater expressivity than tensor networks and autoregressive neural networks, our approach can build on the state-of-the-art performance of these two methods in a variety of further physics applications.

Besides scientific applications, since both tensor networks and autoregressive neural networks have been applied to machine learning tasks such as supervised learning and generative modeling, Autoregressive Neural TensorNet can also be naturally applied to these other contexts. Our novel approach holds promise for better performance in these other domains due to its exact sampling, expressivity, and symmetries.

8. Acknowledgement

The authors acknowledge support from the National Science Foundation under Cooperative Agreement PHY-2019786 (The NSF AI Institute for Artificial Intelligence and Fundamental Interactions, <http://iaifi.org/>). This material is based upon work supported by the U.S. Department of Energy, Office of Science, National Quantum Information Science Research Centers, Co-design Center for Quantum Advantage (C2QA) under contract number DE-SC0012704. The authors acknowledge the MIT SuperCloud (Reuther et al., 2018) and Lincoln Laboratory Supercomputing Center for providing (HPC, database, consultation) resources that have contributed to the research results reported within this paper/report.

References

Adams, C., Carleo, G., Lovato, A., and Rocco, N. Variational monte carlo calculations of $a \leq 4$ nuclei with an artificial neural-network correlator ansatz. *Physical Review Letters*, 127(2), Jul 2021. ISSN 1079-7114. doi: 10.1103/physrevlett.127.022502. URL <https://journals.aps.org/prl/abstract/10.1103/PhysRevLett.127.022502>.

Astrakhantsev, N., Westerhout, T., Tiwari, A., Choo, K., Chen, A., Fischer, M. H., Carleo, G., and Neupert, T. Broken-symmetry ground states of the heisenberg model on the pyrochlore lattice. *Physical Review X*, 11(4), Oct 2021. ISSN 2160-3308. doi: 10.1103/physrevx.11.041021. URL <https://journals.aps.org/prx/abstract/10.1103/PhysRevX.11.041021>.

Barrett, T. D., Malyshev, A., and Lvovsky, A. Autoregressive neural-network wavefunctions for ab initio quantum chemistry. *Nature Machine Intelligence*, 4(4):351–358, 2022.

Capriotti, L., Fubini, A., Roscilde, T., and Tognetti, V. Ising transition in the two-dimensional quantum j_1-j_2 heisenberg model. *Physical review letters*, 92(15):157202, 2004.

Carleo, G. and Troyer, M. Solving the quantum many-body problem with artificial neural networks. *Science*, 355(6325):602–606, 2017. doi: 10.1126/science.aag2302. URL <https://www.science.org/doi/abs/10.1126/science.aag2302>.

Carrasquilla, J., Luo, D., Pérez, F., Milsted, A., Clark, B. K., Volkovs, M., and Aolita, L. Probabilistic simulation of quantum circuits with the transformer, 2019.

Chen, Z., Luo, D., Hu, K., and Clark, B. K. Simulating 2+1d lattice quantum electrodynamics at finite density with neural flow wavefunctions. *arXiv preprint arXiv:2212.06835*, 2022.

Choo, K., Neupert, T., and Carleo, G. Two-dimensional frustrated J_1-J_2 model studied with neural network quantum states. *Phys. Rev. B*, 100:125124, Sep 2019. doi: 10.1103/PhysRevB.100.125124. URL <https://link.aps.org/doi/10.1103/PhysRevB.100.125124>.

Deng, D.-L., Li, X., and Das Sarma, S. Quantum entanglement in neural network states. *Physical Review X*, 7(2), May 2017. ISSN 2160-3308. doi: 10.1103/physrevx.7.021021. URL <http://dx.doi.org/10.1103/PhysRevX.7.021021>.

Ferris, A. J. and Vidal, G. Perfect sampling with unitary tensor networks. *Phys. Rev. B*, 85:165146, Apr 2012. doi: 10.1103/PhysRevB.85.165146. URL <https://link.aps.org/doi/10.1103/PhysRevB.85.165146>.

Gao, X. and Duan, L.-M. Efficient representation of quantum many-body states with deep neural networks. *Nature Communications*, 8(1):662, Sep 2017. ISSN 2041-1723. doi: 10.1038/s41467-017-00705-2. URL <https://www.nature.com/articles/s41467-017-00705-2>.

Girvin, S. M. and Yang, K. *Modern condensed matter physics*. Cambridge University Press, 2019.

Glasser, I., Pancotti, N., August, M., Rodriguez, I. D., and Cirac, J. I. Neural-network quantum states, string-bond states, and chiral topological states. *Physical Review X*, 8(1), Jan 2018. ISSN 2160-3308. doi: 10.1103/physrevx.8.011006.

URL <https://journals.aps.org/prx/abstract/10.1103/PhysRevX.8.011006>.

Greensmith, E., Bartlett, P. L., and Baxter, J. Variance reduction techniques for gradient estimates in reinforcement learning. *J. Mach. Learn. Res.*, 5:1471–1530, December 2004. ISSN 1532-4435.

Gutiérrez, I. L. and Mendl, C. B. Real time evolution with neural-network quantum states, 2020.

Han, X. and Hartnoll, S. A. Deep quantum geometry of matrices. *Physical Review X*, 10(1), Mar 2020. ISSN 2160-3308. doi: 10.1103/physrevx.10.011069. URL <https://journals.aps.org/prx/abstract/10.1103/PhysRevX.10.011069>.

Hartmann, M. J. and Carleo, G. Neural-network approach to dissipative quantum many-body dynamics. *Phys. Rev. Lett.*, 122:250502, Jun 2019. doi: 10.1103/PhysRevLett.122.250502. URL <https://journals.aps.org/prl/abstract/10.1103/PhysRevLett.122.250502>.

Hermann, J., Schätzle, Z., and Noé, F. Deep neural network solution of the electronic schrödinger equation, 2019.

Hibat-Allah, M., Ganahl, M., Hayward, L. E., Melko, R. G., and Carrasquilla, J. Recurrent neural network wave functions. *Phys. Rev. Research*, 2:023358, Jun 2020. doi: 10.1103/PhysRevResearch.2.023358. URL <https://journals.aps.org/prresearch/abstract/10.1103/PhysRevResearch.2.023358>.

Huang, Y. and Moore, J. E. Neural network representation of tensor network and chiral states. *Phys. Rev. Lett.*, 127:170601, Oct 2021. doi: 10.1103/PhysRevLett.127.170601. URL <https://link.aps.org/doi/10.1103/PhysRevLett.127.170601>.

Lami, G., Carleo, G., and Collura, M. Matrix product states with backflow correlations. *Physical Review B*, 106(8), aug 2022. doi: 10.1103/physrevb.106.108111. URL <https://doi.org/10.1103/2Fphysrevb.106.108111>.

Lante, V. and Parola, A. The ising phase in the j1-j2 heisenberg model. *Physical Review*, 2006.

Levine, Y., Sharir, O., Cohen, N., and Shashua, A. Quantum entanglement in deep learning architectures. *Physical Review Letters*, 122(6), Feb 2019a. ISSN 1079-7114. doi: 10.1103/physrevlett.122.065301. URL <https://journals.aps.org/prl/abstract/10.1103/PhysRevLett.122.065301>.

Levine, Y., Sharir, O., Cohen, N., and Shashua, A. Quantum entanglement in deep learning architectures. *Physical review letters*, 122(6):065301, 2019b.

Lu, S., Gao, X., and Duan, L.-M. Efficient representation of topologically ordered states with restricted boltzmann machines. *Phys. Rev. B*, 99:155136, Apr 2019. doi: 10.1103/PhysRevB.99.155136. URL <https://journals.aps.org/prb/abstract/10.1103/PhysRevB.99.155136>.

Luo, D. and Clark, B. K. Backflow transformations via neural networks for quantum many-body wave functions. *Physical Review Letters*, 122(22), Jun 2019. ISSN 1079-7114. doi: 10.1103/physrevlett.122.226401. URL <https://journals.aps.org/prl/abstract/10.1103/PhysRevLett.122.226401>.

Luo, D. and Halverson, J. Infinite neural network quantum states, 2021. URL <https://arxiv.org/abs/2112.00723>.

Luo, D., Carleo, G., Clark, B. K., and Stokes, J. Gauge equivariant neural networks for quantum lattice gauge theories. *Physical review letters*, 127(27):276402, 2021a.

Luo, D., Chen, Z., Hu, K., Zhao, Z., Hur, V. M., and Clark, B. K. Gauge invariant autoregressive neural networks for quantum lattice models, 2021b. URL <https://arxiv.org/abs/2101.07243>.

Luo, D., Chen, Z., Carrasquilla, J., and Clark, B. K. Autoregressive neural network for simulating open quantum systems via a probabilistic formulation. *Phys. Rev. Lett.*, 128:090501, Feb 2022a. doi: 10.1103/PhysRevLett.128.090501. URL <https://link.aps.org/doi/10.1103/PhysRevLett.128.090501>.

Luo, D., Yuan, S., Stokes, J., and Clark, B. K. Gauge equivariant neural networks for 2+ 1d u (1) gauge theory simulations in hamiltonian formulation. *arXiv preprint arXiv:2211.03198*, 2022b.

Martyn, J. M., Najafi, K., and Luo, D. Variational neural-network ansatz for continuum quantum field theory. *arXiv preprint arXiv:2212.00782*, 2022.

Medvidović, M. and Carleo, G. Classical variational simulation of the quantum approximate optimization algorithm. *npj Quantum Information*, 7(1), Jun 2021. ISSN 2056-6387. doi: 10.1038/s41534-021-00440-z. URL <https://www.nature.com/articles/s41534-021-00440-z>.

Nagy, A. and Savona, V. Variational quantum monte carlo method with a neural-network ansatz for open quantum systems. *Phys. Rev. Lett.*, 122:250501, Jun 2019. doi: 10.1103/PhysRevLett.122.250501. URL <https://journals.aps.org/prl/abstract/10.1103/PhysRevLett.122.250501>.

Nomura, Y. and Imada, M. Dirac-type nodal spin liquid revealed by refined quantum many-body solver using neural-network wave function, correlation ratio, and level spectroscopy. *Physical Review X*, 11(3), aug 2021. doi: 10.1103/physrevx.11.031034. URL <https://doi.org/10.1103/physrevx.11.031034>.

Nomura, Y., Darmawan, A. S., Yamaji, Y., and Imada, M. Restricted boltzmann machine learning for solving strongly correlated quantum systems. *Physical Review B*, 96(20), Nov 2017. ISSN 2469-9969. doi: 10.1103/physrevb.96.205152. URL <https://journals.aps.org/prb/abstract/10.1103/PhysRevB.96.205152>.

Oseledets, I. V. Tensor-train decomposition. *SIAM Journal on Scientific Computing*, 33(5):2295–2317, 2011. doi: 10.1137/090752286. URL <https://doi.org/10.1137/090752286>.

Pfau, D., Spencer, J. S., Matthews, A. G. D. G., and Foulkes, W. M. C. Ab initio solution of the many-electron schrödinger equation with deep neural networks. *Phys. Rev. Research*, 2:033429, Sep 2020. doi: 10.1103/PhysRevResearch.2.033429. URL <https://journals.aps.org/prresearch/abstract/10.1103/PhysRevResearch.2.033429>.

Preskill, J. Quantum computing 40 years later. *arXiv preprint arXiv:2106.10522*, 2021.

Reuther, A., Kepner, J., Byun, C., Samsi, S., Arcand, W., Bestor, D., Bergeron, B., Gadepally, V., Houle, M., Hubbell, M., Jones, M., Klein, A., Milechin, L., Mullen, J., Prout, A., Rosa, A., Yee, C., and Michaleas, P. Interactive supercomputing on 40,000 cores for machine learning and data analysis. In *2018 IEEE High Performance extreme Computing Conference (HPEC)*, pp. 1–6. IEEE, 2018.

Schmitt, M. and Heyl, M. Quantum many-body dynamics in two dimensions with artificial neural networks. *Physical Review Letters*, 125(10), Sep 2020. ISSN 1079-7114. doi: 10.1103/physrevlett.125.100503. URL <https://journals.aps.org/prl/abstract/10.1103/PhysRevLett.125.100503>.

Sharir, O., Levine, Y., Wies, N., Carleo, G., and Shashua, A. Deep autoregressive models for the efficient variational simulation of many-body quantum systems. *Physical Review Letters*, 124(2), jan 2020. doi: 10.1103/physrevlett.124.020503. URL <https://doi.org/10.1103/2Fphysrevlett.124.020503>.

Sharir, O., Shashua, A., and Carleo, G. Neural tensor contractions and the expressive power of deep neural quantum states, 2021.

Stokes, J., Moreno, J. R., Pnevmatikakis, E. A., and Carleo, G. Phases of two-dimensional spinless lattice fermions with first-quantized deep neural-network quantum states. *Physical Review B*, 102(20), Nov 2020. ISSN 2469-9969. doi: 10.1103/physrevb.102.205122. URL <https://journals.aps.org/prb/abstract/10.1103/PhysRevB.102.205122>.

Torlai, G., Mazzola, G., Carrasquilla, J., Troyer, M., Melko, R., and Carleo, G. Neural-network quantum state tomography. *Nature Physics*, 14(5):447–450, May 2018. ISSN 1745-2481. doi: 10.1038/s41567-018-0048-5. URL <https://www.nature.com/articles/s41567-018-0048-5>.

Van den Oord, A., Kalchbrenner, N., Espeholt, L., Vinyals, O., Graves, A., et al. Conditional image generation with pixelcnn decoders. In *Advances in neural information processing systems*, pp. 4790–4798, 2016a.

Van den Oord, A., Kalchbrenner, N., Espeholt, L., Vinyals, O., Graves, A., et al. Conditional image generation with pixelcnn decoders. *Advances in neural information processing systems*, 29, 2016b.

Verstraete, F. and Cirac, J. I. Renormalization algorithms for quantum-many body systems in two and higher dimensions, 2004. URL <https://arxiv.org/abs/cond-mat/0407066>.

Vicentini, F., Biella, A., Regnault, N., and Ciuti, C. Variational neural-network ansatz for steady states in open quantum systems. *Physical Review Letters*, 122(25), Jun 2019. ISSN 1079-7114. doi: 10.1103/physrevlett.122.250503. URL <https://journals.aps.org/prl/abstract/10.1103/PhysRevLett.122.250503>.

Vicentini, F., Hofmann, D., Szabó, A., Wu, D., Roth, C., Giuliani, C., Pescia, G., Nys, J., Vargas-Calderón, V., Astrakhantsev, N., and Carleo, G. NetKet 3: Machine learning toolbox for many-body quantum systems. *SciPost Physics Codebases*, aug 2022. doi: 10.21468/scipostphyscodeb.7. URL <https://doi.org/10.21468%2Fscipostphyscodeb.7>.

Vidal, G. Efficient classical simulation of slightly entangled quantum computations. *Physical Review Letters*, 91(14), oct 2003. doi: 10.1103/physrevlett.91.147902. URL <https://doi.org/10.1103/2Fphysrevlett.91.147902>.

Vidal, G. Efficient simulation of one-dimensional quantum many-body systems. *Physical Review Letters*, 93(4), jul 2004. doi: 10.1103/physrevlett.93.040502. URL <https://doi.org/10.1103/2Fphysrevlett.93.040502>.

Vidal, G. Entanglement renormalization. *Phys. Rev. Lett.*, 99:220405, Nov 2007. doi: 10.1103/PhysRevLett.99.220405. URL <https://link.aps.org/doi/10.1103/PhysRevLett.99.220405>.

Vieijra, T., Casert, C., Nys, J., De Neve, W., Haegeman, J., Ryckebusch, J., and Verstraete, F. Restricted boltzmann machines for quantum states with non-abelian or anyonic symmetries. *Physical Review Letters*, 124(9), Mar 2020. ISSN 1079-7114. doi: 10.1103/physrevlett.124.097201. URL <https://journals.aps.org/prl/abstract/10.1103/PhysRevLett.124.097201>.

Wang, J., Chen, Z., Luo, D., Zhao, Z., Hur, V. M., and Clark, B. K. Spacetime neural network for high dimensional quantum dynamics, 2021.

White, S. R. Density matrix formulation for quantum renormalization groups. *Physical review letters*, 69(19):2863, 1992.

Wu, D., Rossi, R., Vicentini, F., and Carleo, G. From tensor network quantum states to tensorial recurrent neural networks. *arXiv preprint arXiv:2206.12363*, 2022.

Yoshioka, N. and Hamazaki, R. Constructing neural stationary states for open quantum many-body systems. *Phys. Rev. B*, 99:214306, Jun 2019. doi: 10.1103/PhysRevB.99.214306. URL <https://journals.aps.org/prb/abstract/10.1103/PhysRevB.99.214306>.

A. Additional Theoretical Proofs

Theorem A.1. *Autoregressive neural network quantum wavefunction is normalized and allows for exact sampling.*

Proof. Define $q(\mathbf{x}) := |\psi(\mathbf{x})|^2$ and $q(x_i|\mathbf{x}_{<i}) := |\psi(x_i|\mathbf{x}_{<i})|^2$. It can be shown that q satisfies Eq. 1. Thus, $q(x_i|\mathbf{x}_{<i})$ is the conditional probability of x_i given $\mathbf{x}_{<i}$. Therefore, the normalization is guaranteed as long as each $q(x_i|\mathbf{x}_{<i}) = |\psi(x_i|\mathbf{x}_{<i})|^2$ is normalized; and exact sampling can be obtained via sampling $x_i \sim q(x_i|\mathbf{x}_{<i})$ for each i . \square

Theorem A.2. *Matrix product state wavefunction is normalized and allows for exact sampling in right canonical form.*

Proof. Define $M_R^{\alpha_{j-1}}(\mathbf{x}_{\geq j}) := \sum_{\alpha_{\geq j}} \prod_{i=j}^n M^{\alpha_{i-1}\alpha_i}(x_i)$ the right partially contracted tensor from site j (We ignored α_{n+1} because it has dimension 1). In the right canonical form, the M tensors are chosen such that

$$\sum_{\mathbf{x}_{\geq j}} M_R^{\alpha_{j-1}}(\mathbf{x}_{\geq j}) M_R^{\alpha'_{j-1}}(\mathbf{x}_{\geq j})^* = \delta_{\alpha_{j-1}\alpha'_{j-1}} \quad \forall j, \quad (18)$$

where $*$ denotes complex conjugation and $\delta_{\alpha\alpha'}$ is the Kronecker delta function that evaluates 1 if $\alpha = \alpha'$ and 0 otherwise. This automatically implies normalization by substituting $j = 1$. Let's also define the left partially contracted tensor as $M_L^{\alpha_j}(\mathbf{x}_{\leq j}) := \sum_{\alpha_{\leq j}} \prod_{i=1}^j M^{\alpha_{i-1}\alpha_i}(x_i)$. In this canonical form, the marginal probability for first j qubits (Fig. 1 (c))

$$q(\mathbf{x}_{\leq j}) = \sum_{\mathbf{x}_{>j}} |\psi(\mathbf{x})|^2 = \sum_{\alpha_j} M_L^{\alpha_j}(\mathbf{x}_{\leq j}) M_L^{\alpha_j}(\mathbf{x}_{\leq j})^*. \quad (19)$$

The conditional probability is then evaluated as $q(x_j|\mathbf{x}_{<j}) = q(\mathbf{x}_{\leq j})/q(\mathbf{x}_{<j})$ (or as a direct renormalization of $q(\mathbf{x}_{\leq j})$ with $\mathbf{x}_{<j}$ fixed), which allows exact sampling. \square

Theorem A.3. *Autoregressive Neural TensorNet inherits function symmetry from autoregressive neural networks.*

Proof. As we discussed in the main paper, we apply the symmetry on the left partially contracted tensors instead of the conditional probabilities. Here, we show that this produces the desired conditional probabilities and phase. Applying the function symmetry on the left partially contracted tensors results in

$$\tilde{\psi}_L^{\alpha_j}(\mathbf{x}_{\leq j}) = \tilde{\psi}_L^{\alpha_j}(F(\mathbf{x}_{\leq j})). \quad (20)$$

After contracting over the index α_j , this implies $q(\mathbf{x}_{\leq j}) = q(F(\mathbf{x}_{\leq j}))$, which then implies

$$q(x_j|\mathbf{x}_{<j}) = q(F(x_j)|F(\mathbf{x}_{<j})), \quad (21)$$

as conditional probability is just the marginal probability normalized at site j . The phase, on the other hand,

$$\phi(\mathbf{x}) = \text{Arg} \sum_{\alpha} \prod_{i=1}^n \tilde{\psi}^{\alpha_{i-1},\alpha_i}(x_i|\mathbf{x}_{<i}) = \text{Arg} \tilde{\psi}_L^{\alpha_n}(\mathbf{x}_{\leq n}), \quad (22)$$

which satisfies the same function symmetry. \square

B. Additional Benchmarks

Before showing additional data, we would like to first explain a technical point. The Heisenberg model (as well as the J_1 - J_2 model) has a sign problem such that the ground state wave function is not positive. This poses serious problems for quantum Monte Carlo as well as existing neural network algorithms. At $J_2 = 0$, the solution to the sign problem is known as the Marshall sign rule, which analytically precalculates the sign of each wave function amplitude. For $J_2 \neq 0$, the sign rule becomes inaccurate. However, it is believed that for small J_2 , the sign rule could still improve result. Previous neural network algorithms typically uses the Marshall sign rule as it is typically not possible to obtain good results without it. But, for previous simulations reported in our paper's table, we did not use the Marshall sign rule. This is also one advantage of our ANTN as tensor networks usually can represent such signs without the sign rule. By starting with an MPS solution, our neural network has significantly less difficulty in representing the ground state wave function.

To address the concern on our previous PixelCNN performance, we would like to point out that its worse performance is also related to lack of sign rule (we now provide the PixelCNN with sign rule of better performance). We also include

$J_2 = 0.2$	DMRG (1024)	DMRG (70)	DMRG (8)	PixelCNN	PixelCNN (sign)
8×8	-2.236804	-2.192334	-2.001620	-2.21218(16)	-2.23171(9)
$J_2 = 0.2$	Elementwise (8)	Blockwise (70)	RBM (3)	RBM (3 sign)	
8×8	-2.23690(4)	-2.23484(73)	-1.9609(16)	-2.1944(17)	
$J_2 = 0.5$	DMRG (1024)	DMRG (70)	DMRG (8)	PixelCNN	PixelCNN (sign)
8×8	-1.934127	-1.885860	-1.735175	-1.77058(29)	-1.88902(19)
$J_2 = 0.5$	Elementwise (8)	Blockwise (70)	RBM (3)	RBM (3 sign)	MPBS
8×8	-1.93018(8)	-1.93000(7)	-1.5128(20)	-1.8625(20)	-1.9267
$J_2 = 0.8$	DMRG (1024)	DMRG (70)	DMRG (8)	PixelCNN	PixelCNN (sign)
8×8	-2.016361	-1.967760	-1.833780	-1.93825(16)	-1.83672(26)
$J_2 = 0.8$	Elementwise (8)	Blockwise (70)	RBM (3)	RBM (3 sign)	
8×8	-2.00036(16)	-1.99148(13)	-1.7508(19)	-0.7267(29)	

Table 2. Additional comparisons for 8×8 system. The "sign" inside the parenthesis denotes the usage of the sign rule. The number inside the parenthesis indicates bond dimension for DMRG and ANTN, and indicates ratio between hidden and visible units for RBM.

the Restricted Boltzmann Machine (RBM) with/without sign rule (hidden/input ratio=3) using the standard library Netket (Vicentini et al., 2022) in the field for comparison.

In Table 2, we provide additional data for 8×8 system. We compare our results with the out-of-box RBM implemented in NetKet (Vicentini et al., 2022). For $J_2 = 0.5$, we in addition compare the recent MPBS (Lami et al., 2022) result. We observe that while the sign rule significantly improves the PixelCNN result for $J_2 = 0.2$ and $J_2 = 0.5$, it makes the result at $J_2 = 0.8$ much worse. In addition, the PixelCNN with sign rule is as good as neither the elementwise nor the blockwise ANTN. The out-of-box RBM result with $\alpha = 3$ (192 hidden units) is also not as good as our neural network.

DMRG (1024)	DMRG (70)	DMRG (8)	PixelCNN	PixelCNN (sign)
-2.509307	-2.451369	-2.258612	-2.50466(9)	-2.51187(6)
Elementwise (8)	Elementwise (8 sign)	Elementwise (24)	Elementwise (24 sign)	Blockwise (70)
-2.51421(3)	-2.51437(3)	-2.51442(1)	-2.51447(1)	-2.51248(4)
RBM (3)	RBM (3 sign)	PixelCNN2	TensorRNN (40 sign)	TensorRNN (60 sign)
-1.9193(10)	-2.4765(13)	-2.514508(4)	-2.514112	-2.514434

Table 3. Additional comparisons for 10×10 system at $J_2 = 0$. The "sign" inside the parenthesis denotes the usage of the sign rule. The number inside the parenthesis indicates bond dimension for DMRG and ANTN, and indicates ratio between hidden and visible units for RBM.

In Table 3, we compare our neural network with other works as well as the out-of-box RBM from NetKet (Vicentini et al., 2022) with $\alpha = 3$ (300 hidden units) for 10×10 system at $J_2 = 0$ (Heisenberg model). While our implementation of PixelCNN is slightly worse compared to PixelCNN2 (Carleo & Troyer, 2017), we believe it mainly comes down to (a), we used only 7 layers while the previous work used 20 layers, and (b), we didn't fine tune the training while the previous work used sophisticated training method. Moreover, our elementwise ANTN result (especially with bond dimension of 24) is comparable with the current state of the art from both the previous pixelCNN and the TensorRNN. We also note that our ANTN is not sensitive to the sign rule as the result suggests. We further note that our construction is not limited to our implementation of PixelCNN and MPS. We notice that since the TensorRNN (Wu et al., 2022) is actually more similar to a 2D tensor network than a neural network and it permits autoregressive sampling, using our ANTN construction, it is possible to implement more powerful ansatz by replacing the PixelCNN in our implementation with a more powerful one and replacing the MPS with TensorRNN to further improve the results.

C. Additional Details for Exact Sampling

In this work, our pixelCNN is implemented following the gated version of (Van den Oord et al., 2016a; Chen et al., 2022). The pixelCNN was used as an autoregressive model for image generation purposes. In each layer, the Gated pixelCNN contains a horizontal branch and a vertical branch, where the convolutional kernels are masked such that the vertical branch

only sees the qubits (or pixels) in the previous rows, while the horizontal branch sees the previous qubits (or pixels) in the same row. The information is combined at each layer from the vertical branch to the horizontal branch to obtain the full information of previous qubits. This masking implicitly creates a zig-zag order that generates a conditional probability distribution (or conditional tensor that turns into a probability distribution). More specifically, in this order, x_1 would be the qubit at $(1, 1)$, x_2 would be the qubit at $(1, 2)$, x_{L_y+1} would be the qubit at $(2, 1)$, and $x_{L_x \times L_y}$ would be the qubit at (L_x, L_y) . We put the MPS in the same zig-zag order. This allows us to perform exact sampling by sampling sequentially from the conditional distributions $p(x_i | x_{<i})$ in the same zig-zag order.

D. Additional Experimental Details

The PixelCNN used in this work is the same as (Chen et al., 2022) without the channel wise mask. The neural network has 7 layers with dilations 1, 2, 1, 4, 1, 2 and 1 for each layer and a hidden dimension of 48. PixelCNN has an effective bond dimension of 1; elementwise ANTNs use a bond dimension of 8; blockwise ANTNs use a bond dimension of 70.

To train the three neural networks, we begin from scratch with the 4×4 system size. For larger system sizes of $N \times N$, we use transfer learning from the trained model on a system size of $(N - 2) \times (N - 2)$ by keeping all but the weights in the last layer. The models are trained on 2 GPUs on an Intel Xeon Gold 6248 processor from MIT’s SuperCloud cluster (Reuther et al., 2018).

The parameters are initialized with PyTorch’s default initialization scheme for CNN. For ANTN, we load the DMRG result with the corresponding system size and bond dimension at the beginning of the training.

We use the Adam optimizer with a initial learning rate of 0.01. The learning rate is halved at steps 100, 500, 1000, 1800, 2500, 4000, 6000, and 8000. For system sizes of 4×4 up to 12×12 , respectively, we train for 5000, 5000, 4000, 3000, and 2000 steps. The effective batch size (batch size \times accumulation steps \times number of GPUs) is 10000 throughout the training.